

# NATIONAL AIR INTELLIGENCE CENTER



SELECTED ARTICLES

DTIC QUALITY INSPECTED 4



Approved for public release:  
distribution unlimited

19960619 009

**HUMAN TRANSLATION**

NAIC-ID(RS)T-0136-96 2 May 1996

MICROFICHE NR: 96000363

SELECTED ARTICLES

English pages: 28

Source: Qiangjiguang Yu Lizishu (High Power Laser and Particle Beams), Vol. 3, Nr. 3, August 1991; pp. 297-302; 323-330

Country of origin: China

Translated by: Leo Kanner Associates  
F33657-88-D-2188

Requester: NAIC/TATD/Bruce Armstrong

Approved for public release: distribution unlimited.

THIS TRANSLATION IS A RENDITION OF THE ORIGINAL FOREIGN TEXT WITHOUT ANY ANALYTICAL OR EDITORIAL COMMENT STATEMENTS OR THEORIES ADVOCATED OR IMPLIED ARE THOSE OF THE SOURCE AND DO NOT NECESSARILY REFLECT THE POSITION OR OPINION OF THE NATIONAL AIR INTELLIGENCE CENTER.

PREPARED BY:

TRANSLATION SERVICES  
NATIONAL AIR INTELLIGENCE CENTER  
WPAFB, OHIO

## TABLE OF CONTENTS

Graphics Disclaimer .....	ii
FAST ALGORITHM OF ZONAL WAVEFRONT RECONSTRUCTION, by Wang Yingbo .....	1
MIXING PROCESSES DOWNSTREAM OF NOZZLE BANK OF A SUPERSONIC CW HF/DF LASER, by Sang Fenting, Gou Chenzhou, Zhuang Qi, Xie Xingbing, Yuan Qinian, Huang Ruiping, Zhuang Cunhao .....	16

#### GRAPHICS DISCLAIMER

All figures, graphics, tables, equations, etc. merged into this translation were extracted from the best quality copy available.

## FAST ALGORITHM OF ZONAL WAVEFRONT RECONSTRUCTION

Wang Yingbo

Beijing Institute of Technology

**ABSTRACT** This paper describes a fast algorithm —sub—block wave—front reconstruction. It has characteristics of smaller required memory capacity, smaller noise coefficient and better numerical value stability. Because of new errors of the algorithm, qualitative analysis and computer simulation results indicate that its reconstruction precision is basically equal to that of the usual algorithm.

**KEY WORDS** adaptive optics, wave—front reconstruction, zonal method.

### I. Introduction

One of the key problems in adaptive optics is how to obtain the data reconstruction wavefront from the wavefront detector. Commonly used reconstruction algorithms include the zonal reconstruction method and the mode reconstruction method. In the zonal reconstruction method, the Southwell approach [1] is suitable for a Hartmann detector with higher reconstruction accuracy. Here, the measured inclination rate and the phase point to be estimated are on lattice points. The phase solution can be summarized in the following linear algebraic equation set:

In the equation,  $S$  is the inclination vector for two orthogonal directions;  $\Phi$  is the phase to be estimated;  $D$  is a sparse matrix; and  $A$  is the matrix related to the algorithm and the lattice-point layout. Eq. (1) is a constant equation. The minimum norm solution of the least-squares of  $\Phi$  is

$$A\Phi = DS \quad (1)$$

If we let  $B=A^{-D}$ , then

$$\Phi = A^{-D}DS \quad (2)$$

$$\Phi = BS \quad (3)$$

$A^{-}$  is the Moore-Penrose inverse of  $A$  in the broad sense. After determining the system parameters,  $B$  can be determined off-line for storage.

If the number of the subapertures is  $N \times N$ , then  $B$  is the  $N^2 \times 2N^2$  matrix. The total computational volume in computing Eq. (3) is  $2N^4$  times the multiplication and addition operations, with storage of  $2N^4$  elements. Since the computational volume and storage are relatively high, it is more difficult to conduct real-time wavefront reconstruction. Based on the features of the zonal method, the article presents a method of fast calculation of  $\Phi$ .

## II. Subblock Wavefront Reconstruction Method

The principle of the zonal reconstruction method is to apply the measured inclination rate (not exceeding four points at the maximum) of adjacent positions of the phase point to be estimated for interpolation to obtain the wavefront phase. If it is assumed that the post-subblock boundary effect of the subaperture

array can be approximately neglected, the wavefront reconstruction carried out independently for various blocks with the addition of the determined revised value is equivalent to the above-mentioned conventional algorithm. Thus, the computational volume can be reduced without bringing about a greater effect on the estimation accuracy. This is the fundamental concept of subblock wavefront reconstruction.

Let us assume that there is a square subaperture array with  $N \times N$  subapertures, which are divided into several square subblocks. Let  $k$  and  $n$  indicate, respectively, the number of subblocks in the horizontal direction, and the number of subapertures in the horizontal direction in each block; obviously,  $N=nk$ .

After subblocking, the wavefront reconstruction equation of various blocks can be written as:

$$A_{ij} \Phi_{ij} = D_{ij} S_{ij} \quad (4)$$

$$\Phi_{ij} = A_{ij}^* D_{ij} S_{ij} = B_{ij} S_{ij} \quad (5)$$

$(i=1, 2, \dots, k, j=1, 2, \dots, k)$

Since the sizes of the subdivided blocks are homogeneous and equal to each other,  $B_{ij}$  of the various blocks are the same.

Therefore, let

$$G_{n^2 \times 2n^2} = B_{ij} \quad (6)$$

$$\Phi_{ij} = G S_{ij} \quad (7)$$

The phase values obtained from Eqs. (3) and (7) are not consistent. This is because both solutions to the equations have the minimum-norm feature. In other words, the mean value of the

phases is zero. After subblocking, this approach will lead to a difference of a constant between the subblocked reconstruction phase and the reconstruction phase under the conventional algorithm. Therefore, to ensure continuity of the wavefront,  $\Phi_{ij}$  in Eq. (7) should have a revision value added to it, which should be the difference between the reconstruction phase value of a specific point in the conventional algorithm, and the subblock reconstruction phase value at the point. In other words,

$$d_{ij} = \Phi(i', j') - \Phi_{ij}(i', j') \quad (8)$$

In the equation,  $i(k-1) < i' < ik$ ,  $j(i-1) < j' < jk$ .

The point  $(i', j')$  should be located at the center position ( $n$  is an odd number) or near the center position ( $n$  is an even number) of the subblock. Thus, since the number of related points of the adjacent zones is unaffected by subblocking, the phase estimation accuracy at this point is not affected.

From Eq. (3), we know that  $\Phi(i', j')$  in Eq. (8) indicates the specific weighting summation of vector  $S$ . In other words,

$$\Phi(i', j') = b^T(i', j') S \quad (9)$$

On the same line of reasoning, from Eq. (7) we know that  $\Phi_{ij}(i', j')$  can be used to indicate the specific weighting of vector  $S_{ij}$ . In other words,

$$\Phi_{ij}(i', j') = g_{ij}^T(i', j') S_{ij} \quad (10)$$

Since  $S_{ij}$  is a subset of  $S$ , Eq. (10) can be rewritten as:

$$\Phi_{ij}(i', j') = l_{ij}^T(i', j') S \quad (11)$$

In the equation,  $l_{ij}^T(i', j')$  corresponding to the  $S_{ij}$  portion of the  $S$  vector is the element of  $g_{ij}^T(i', j')$ , the others are equal to



zero.

$$\text{If we let } h_{ij}^T = b^T(i', j') - l_{ij}^T(i', j') \quad (12)$$

$$\text{then } d_{ij} = h_{ij}^T S \quad (13)$$

If the following equations are introduced,

$$d = \begin{bmatrix} d_{11} \\ d_{12} \\ \vdots \\ d_{kk} \end{bmatrix}_{k^2 \times 1} \quad H = \begin{bmatrix} h_{11}^T \\ h_{12}^T \\ \vdots \\ h_{kk}^T \end{bmatrix}_{k^2 \times 2N^2} \quad I = \begin{bmatrix} 1 \\ 1 \\ \vdots \\ 1 \end{bmatrix}_{n^2 \times 1}$$

Then Eq. (13) can be rewritten as

$$d = HS \quad (14)$$

After revision, the phase value can be indicated as

$$\Phi'_{ij} = \Phi_{ij} + d_{ij} \cdot I \quad (i=1, 2, \dots, k, \quad j=1, 2, \dots, k) \quad (15)$$

With respect to the adaptive-optics system applying the zonal method, since the subapertures and the drivers correspond to each other,  $\Phi_{ij}$  need not be calculated. It is required only to add a specific DC bias to all drivers in the corresponding subblock after obtaining  $d_{ij}$ .

Then the subblock wavefront reconstruction can be summarized as requiring the calculation of Eqs. (7) and (14). If it is assumed that the ratios between the computational volume and the storage, on the one hand, and the corresponding values in the conventional algorithm Eq. (3) are, respectively,  $p$  and  $q$ , then it is easy to obtain the following:

$$p = \frac{k^2 \cdot 2n^4 + 2k^2 N^2}{2N^4} = \frac{1}{k^2} + \frac{1}{n^2} \quad (16)$$

$$q = \frac{2n^4 + 2k^2 N^2}{2N^4} = \frac{1}{k^2} + \frac{1}{n^2} \quad (17)$$

For a given  $N$ , by selecting equal values or close to equal values between  $k$  and  $n$ , the value of  $p$  can be minimized. From Eqs. (16) and (17), we know that when  $N$  is greater, the computational volume and the storage of the subblock reconstruction method are reduced by more than under the conventional algorithm. For example, when  $N=20$ , by using  $k=4$  and  $n=5$ , then  $p$  is approximately equal to 0.1 and  $q$  is approximately equal to 0.4. Only when  $N$  is greater than or equal to 20, are the reduced amplitudes one order of magnitude or more.

### III. Error Analysis and Computer Simulation

With respect to the subblock wavefront reconstruction algorithm, now the problem of greatest concern is what the accuracy is. In the wavefront reconstruction process, there are two primary sources of error. One is the sampling error because of a limited number of subapertures, and the other is the measurement error. The effect on the phase estimation accuracy can be evaluated by using the noise propagation coefficient, which is defined as the ratio between the phase square error and the measured square error of the phase difference [1]. The expression equation is

$$C(N) = \frac{1}{(Nh)^2} \sum_m \sum_n B_{mn}^2 \quad (18)$$

$B_{mn}$  is the element of matrix  $B$  in Eq. (3).  $h$  is the spacing between subapertures. In the following, the derivation and calculations of the noise propagation coefficient in the subblock reconstruction method are carried out. First, the following symbols are introduced:

$$H_{ij} = \begin{bmatrix} h_{i1}^T \\ h_{i2}^T \\ \vdots \\ h_{iN}^T \end{bmatrix}_{n^2 \times 2N^2} \quad S' = \begin{bmatrix} S_{11} \\ S_{12} \\ \vdots \\ S_{Nk} \end{bmatrix}_{2N^2 \times 1} \quad \Phi' = \begin{bmatrix} \Phi_{11} \\ \Phi_{12} \\ \vdots \\ \Phi_{Nk} \end{bmatrix}_{N^2 \times 1} \quad H' = \begin{bmatrix} H_{11} \\ H_{12} \\ \vdots \\ H_{Nk} \end{bmatrix}_{N^2 \times 2N^2}$$

From Eqs. (13) and (15), we have

$$d_{ii} \cdot I = H_{ii} S \quad (19)$$

Rearrange vector  $S$  so that it becomes  $S'$ . Moreover, corresponding interchanges of various roles in the  $H_{ij}$  matrix are carried out so that the product of the converted  $H'$  subject and vector  $S'$  is the same. In other words,

$$d_{ii} \cdot I = H'_{ii} S' \quad (20)$$

From Eqs. (7) and (15), we know that the revised phase value can be expressed as:

$$\begin{aligned} \Phi' &= \begin{bmatrix} G & & & \\ & G & & 0 \\ & & \ddots & \\ 0 & & & G \end{bmatrix} S' + H' S' \\ &= G' S' + H' S' \end{aligned} \quad (21)$$

Let 
$$B' = G' + H' \quad (22)$$

Then we have 
$$\Phi' = B' S' \quad (23)$$

Assume that the noise propagation coefficient in the subblock reconstruction method is  $C_k(N)$ , then from Eq. (18) and the foregoing equations, we have

$$C_k(N) = \frac{1}{(Nh)^2} \sum_m \sum_n (B_{mn})^2 \quad (24)$$

After computation, the variation status of  $C_k(N)$  with  $N$  and  $k$  is shown in Fig. 1. In the figure,  $k=1$  is equivalent to the

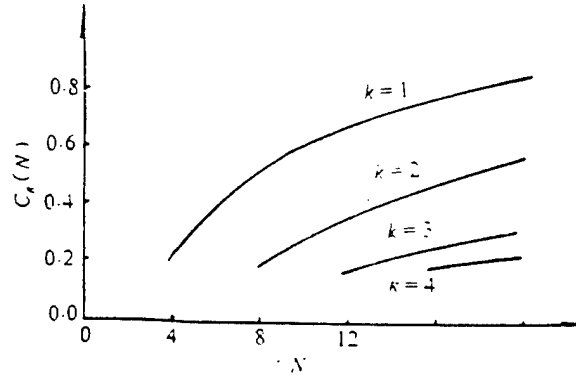


Fig. 1 The curves of the noise propagation coefficient

situation in the conventional algorithm. From the figure we can see that the propagation coefficient in the subblock reconstruction method should be smaller than in the conventional algorithm.

The number of conditions for solving Eq. (3) can reflect the effective degree on the phase solution with perturbation in the B-matrix and the inclination rate. The effective degree is

defined as:

$$\text{cond}(N) = \sigma_{\max} / \sigma_{\min} \quad (25)$$

In the equation,  $\sigma_{\max}$  and  $\sigma_{\min}$  are, respectively, the maximum and the minimum singularities in matrix B. if it is assumed that the number of conditions for solving Eq. (7) for subblocks after subblocking is the condition  $\text{cond}_k(N)$ , then we can obtain

$$\begin{aligned} \text{cond}_k(N) &= \text{cond}(n) \\ &= \text{cond}(N/k) \quad (26) \end{aligned}$$

Since the number of conditions increases rapidly with increased variation, the number of conditions for solving the equation is reduced after subblock reconstruction, then the stability of the values can be enhanced. Fig. 2 shows the

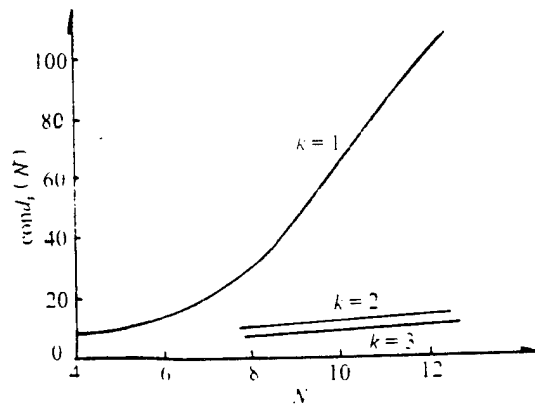


Fig. 2 The curve of the condition number

variation of  $\text{cond}_k$  with  $N$  and  $k$ ;  $(k-1)$  is equivalent to the situation in the conventional algorithm. As indicated by analyzing two aspects of the noise propagation coefficient and the number of conditions mentioned above, it appears that the

subblock reconstruction should lead to smaller wavefront reconstruction errors. However, on the other hand, the consequence of subblocking will reduce the correlated reconstruction points of the phase point of the block and at the block boundaries. To some extent, this will lead to greater reconstruction error.

To examine the effect of the two factors mentioned above on subblock reconstruction accuracy, the author and his colleagues conducted computer simulation. During simulation, a square zone with half a side equal to 1 serving as the aperture, and the numbers of subapertures along the horizontal direction are, respectively,  $N=8$  and  $N=6$ ; along the horizontal direction, the number of subblocks  $k=2$ . Let us assume that the wavefront phase developed by the Zernike polynomial is the summation of the aperture mode of 26 previous orders [2].

$$\Phi(x, y) = \sum_{j=0}^{25} a_j z_j(x, y) \quad (27)$$

Due to the symmetry of aberrations and origins of various orders, we can only calculate the reconstruction mean-square error of the subblocks at the upper left-hand corner; the simulation procedures and methods are shown in the following equations.

$$S_x = \frac{\partial}{\partial x} z_j(x, y) \quad (28)$$

$$S_y = \frac{\partial}{\partial y} z_j(x, y) \quad (29)$$

$$S_{11} = \begin{bmatrix} S_x \\ S_y \end{bmatrix} \quad (30)$$

$$\Phi_{11} = GS_{11} \quad (31)$$

$$d_{11} = h_{11}^T S \quad (32)$$

$$\Phi'_{11} = \Phi_{11} + d_{11} \cdot I \quad (33)$$

$$\sigma_j = \sqrt{\text{Var}(Z_j(x, y) - \Phi_{11})} \quad , \quad j=0, 1, 2, \dots, 25 \quad (34)$$

In the equations,  $S_x$  and  $S_y$  are, respectively, the mean inclination rates upward of the x- and y-directions in the subapertures. By using the mean-square error during reconstruction in the conventional algorithm, we can calculate with the same reasoning.

The simulation results are summarized as follows:

(1) With respect to translation, inclination, defocussing, astigmatism, and other low-order aberrations, the reconstruction mean-square errors in both algorithms are approximately zero. This is because these wavefronts can be precisely reconstructed with the Southwell approach.

(2) With respect to the coma aberration, and the vast majority of aberration modes higher than coma aberration, the reconstruction mean square errors of both algorithms are approximately equal to each other (with an accuracy to one-thousandth of a wavelength).

(3) In the aberration modes in the previous 26 orders, there are only six modes with subblock reconstruction mean-square error relatively increasing over the case with the conventional

algorithm. However, the increasing proportion does not exceed 5%, or the absolute values are smaller. Table 1 lists the simulation results of these six modes.

Table 1 The rms error of wavefront reconstruction  $\sigma$  (unit : wavelength)

aberration algorithm		$Z_{15}$	$Z_{16}$	$Z_{18}$	$Z_{20}$	$Z_{21}$	$Z_{24}$
$N=8$	normal	0.005	0.251	0.251	0.033	0.033	0.556
	in groups	0.025	0.261	0.261	0.046	0.046	0.561
$N=6$	normal	0.008	0.424	0.424	0.054	0.054	0.922
	in groups	0.043	0.442	0.442	0.079	0.079	0.932

(4) In both algorithms, the reconstruction mean-square errors increase synchronously with a reduction in  $n$ . This indicates that the magnitude of  $N$  (the wavefront sampling density) is the main factor determining the reconstruction error.

The above-mentioned applies to a case in the absence of noise. Furthermore, simulation computations are also carried out by adding white noise of gaussian distribution to the inclination data. The signal-to-noise ratio (S/N) are, respectively, taken as 30, 20, and 10dB. When S/N=20dB, other than the six above-mentioned aberration modes with subblock reconstruction mean error slightly greater than that in the conventional algorithm, most other aberration modes indicate a phenomenon with smaller values than the latter. This is because the propagation coefficient of subblock reconstruction noise is smaller and the value stabilization is good. When S/N=30dB, the situation is



close to that in the absence of noise. The situation is in the mid-range when  $S/N=20\text{dB}$ .

As indicated by the  $Z_j(x,y)$  linear summation expression equation for wavefronts in Eq. (27), and the above-mentioned computer simulation results, reconstruction accuracy in the subblock reconstruction algorithm is basically as that in the conventional algorithm; the accuracies may possibly be slightly higher in the presence of intensive noise.

#### IV. Discussion

As pointed out by Southwell [1], with respect to high-order aberrations in wavefronts, the mathematical model proper determines that a better reconstruction effect cannot be obtained. However, this result is determined by the value of  $N$ , the number of subapertures. Affected by atmospheric turbulence perturbations, the power spectrum of the wavefront phase rapidly decreases with increasing spatial frequency (this also can be considered as the number of orders of the aperture modes) [2]. Therefore, the low-order apertures are in the predominant position in the wavefront phase. As indicated in the computer simulation results, with a higher number of orders of the aberration mode, the reconstruction errors in the subblock reconstruction method and in the conventional algorithm increase synchronously with not much difference in the increasing amplitude. Here, both errors can only be reduced by increasing the number of apertures. Since the number of subapertures is

limited, the wavefront detector can detect only the wavefront error in the limited aberration modes. The foregoing discussion can explain that the major errors are unable to appear in the subblock reconstruction method in various situations (especially with high-order aberrations) and the properties in the conventional algorithm.

What has been discussed in the preceding sections has been the evenly divided reconstruction situation of  $N=nk$ . In practice, the method can be extended to the situation when  $N$  is an arbitrary positive integer. Only by dividing  $N$  into the summation of several numbers close to each other, and slightly revising the subblock reconstruction algorithm, can fast wavefront reconstruction still be carried out, but only somewhat increased in the storage volume over that in the evenly divided situation. For example,  $N=17$ ; this can be subblocked based on  $N=4+4+4+5$ . Here, two types of matrix  $G$  in Eq. (7) should be stored in advance.

The Fried method and the Hudgin method are also zonal wavefront reconstruction methods [1]. The main difference from the Southwell approach is the different matrix  $B$  in Eq. (3). Therefore, the subblock wavefront reconstruction method in this article is easily extended to the two above-mentioned approaches; close results are likely to be obtained.

There is always some time delay in the adaptive-optics system; this is one of the main factors affecting its dynamic properties. However, there is quite a sizable proportion in the

total time delay when using the wavefront reconstruction. The subblock wavefront reconstruction can effectively reduce this portion of time, thus enhancing the effect for wavefront correction, and the response rate of the overall system.

## V. Preliminary Conclusions

In the article, the properties of the zonal method are the basis for presenting a fast algorithm, the subblock wavefront reconstruction method. The problems of computational volume, storage quantity, and reconstruction accuracy are analyzed with computer simulation. Compared to the conventional algorithm, there are advantages of greatly reducing computational volume, smaller storage requirement, smaller noise propagation coefficient, and stabilization of values. After analysis, the reconstruction accuracy is basically the same as the latter case.

The author expresses his gratitude to professor Zhou Renzhong, for his advice in the writing of this article. The first draft of the article was received on August 1, 1990; the final revised draft was received for publication on October 25, 1990.

MIXING PROCESSES DOWNSTREAM OF NOZZLE BANK  
OF A SUPERSONIC CW HF/DF LASER

Sang Fenting, Gou Chenzhou, Zhuang Qi, Xie  
Xingbing, Yuan Qinian, Huang Ruiping, and  
Zhuang Cunhao

Dalian Institute of Chemistry and Physics  
Chinese Academy of Sciences

**ABSTRACT** The influence of the design parameters, the structure of the nozzle array as well as the mode of  $H_2$  addition on the output power are discussed. A specific power of 130J/g has been obtained with a mixing distance of 1.75mm between the primary and secondary nozzles.

**KEY WORDS** chemical laser, combustion driven HF chemical lasers, nozzle array, mixing distance, mode of  $H_2$  addition.

## I. Foreword

Since the development of the first continuous-wave HF chemical laser by Spencer et al. in 1969, due to its advantages of high efficiency, small size, no need for external power supply, and short wavelength, there have been rapid developments in CW HF chemical lasers. In 1989, ignition was successful for the HF chemical laser device, which was code-named ALPHA, as a space-based laser weapon in the United States. Its power reached 2MW.

The combustion-driven CW HF (DF) chemical laser device mainly includes five components (Fig. 1): gas intake system,

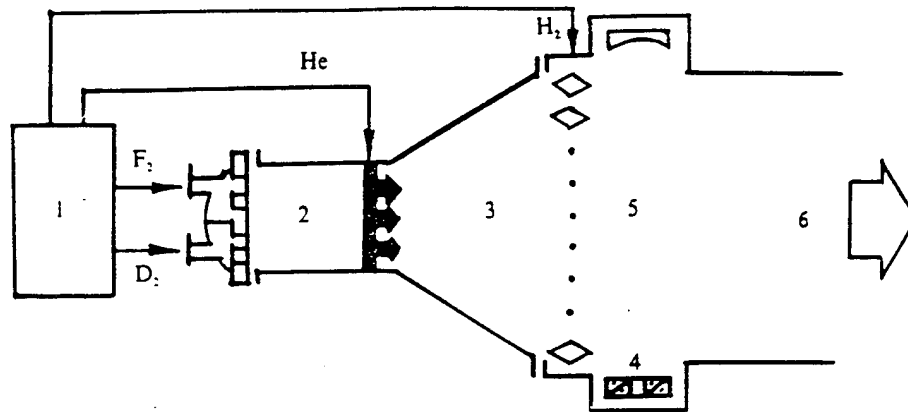


Fig.1 Schematic of CW HF (DF) chemical laser

1. gas control system 2. combustor 3. nozzle 4. mirror 5. laser cavity 6. exhaust system

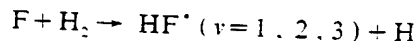
combustion chamber, nozzle bank, optical cavity, and exhaust gas system. Controlled by the gas intake system,  $F_2$  and  $D_2$  enter from the head portion of the combustion chamber to be mixed and burned. From the combustion, high temperature splits the excess  $F_2$  into F atoms, which are diluted with He and accelerated through the nozzle to enter the optical cavity. At the laser cavity inlet, the atoms mix with the cavity fuel  $H_2$  to form oscillating excited-state HF molecules, emitting an HF laser beam in the optical cavity. After processing in the gas exhaust system, exhaust gas is expelled into the atmosphere. The properties of the gas intake system and the combustion chamber, nozzle, optical cavity, and gas exhaust system directly affect laser device performance, especially the nozzles. The properties

not only determine the gas dynamic process of the entire laser cavity, but also has a direct effect on laser beam quality. Therefore, the design, machining, and experimentation on nozzles have been consistently of interest to researchers. The article investigates mainly the effect on performance of output power and specific power (power generated per unit working body flow) of the laser device due to various parameters of the three-dimensional nozzle bank.

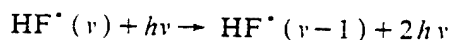
## II. Nozzle Design

Downstream of the laser cavity intake (the plane at the nozzle exit) there are the four following fundamental processes: (1) flowing out of the primary nozzles, the ultrasonic gas flow containing F and He atoms has a diffusional mixing process with the H<sub>2</sub> flow out of the secondary nozzles.

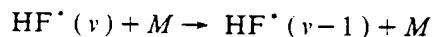
(2) The chemical reaction process (generating the emission working particles) is the chemical pump process:



(3) excitation and emission process:



(4) collision relaxation process:



where M can be HF, H<sub>2</sub>, He, or F<sub>2</sub>.

In the foregoing process, the chemical reaction process proceeds very rapidly measured in the order of microseconds. However, the diffusional mixing process is very slow, measured in

milliseconds. Therefore, the rate of diffusional mixing directly affects the amount of  $\text{HF}^*$  molecules in the oscillating excited state. In other words, speeding up the diffusional mixing process can raise the laser device output power.

If we neglect the wall thickness at the nozzle exit, the diffusion mixing process downstream of the nozzle exit plane can be simplified as shown in Fig. 2.

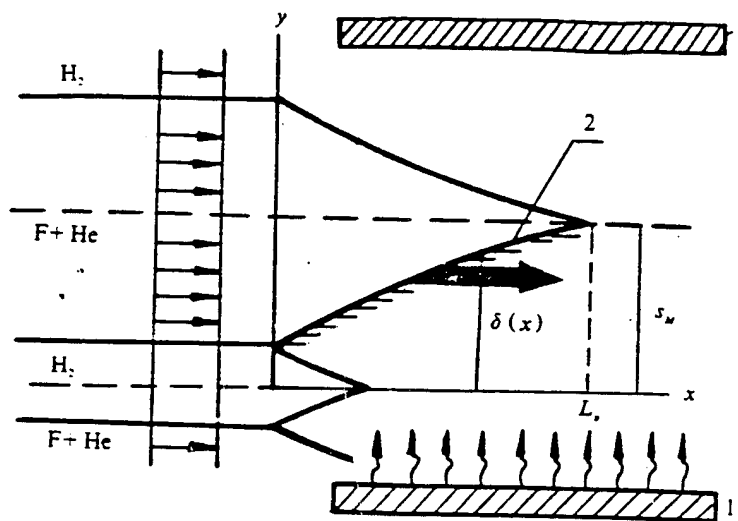


Fig.2 Schematic of mixing layer structure  
1. mirror 2. mixing boundary layer

In the figure,  $L_p$  is the characteristic mixing length, which is the axidirectional length when the cavity fuel  $\text{H}_2$  diffuses to the primary nozzle center line.  $S_M$  is the spacing between the main and the secondary nozzles called the lateral-direction mixing distance.

During the experiments, the laser cavity pressure  $p_e$  is

generally between 0.4 and 0.6kPa; the length  $x$  of the laser emission zone is above 5cm. Based on the results of Shackleford's experiments [1], the flowing state is laminar-flow mixing. The thickness  $\sigma(x)$  of the laminar mixing level can be calculated with the following equation:

$$\sigma(x) = K \left( \frac{DX}{u} \right)^{1/2} \quad (1)$$

In the equation,  $K$  is a constant of the first order of magnitude.  $D$  is the diffusion coefficient. From [2], when  $H_2$  diffuses to such gas current with He as the diluent,  $D$  is  $2.88 \times 10^{-4} (T/p)^{3/2}$ . However,  $T$  and  $p$  are the gas flow temperature and pressure;  $u$  is the gas flow rate. From gas dynamics we know that the supersonic

gas flow rate is  $u = \sqrt{\frac{2\gamma}{\gamma-1} R(T_0 - T)}$ ;  $\gamma$  is the specific-heat ratio, and  $R$  is the gas constant.

From the figure, we know that when  $X=L_D$ ,  $\delta(x)=S_M$ . Here Eq. 1 can be converted to  $L_D = K' S_M \left( \frac{p}{T} \right)^{1/2}$ . From the equation, we know that there are relationships in the diffusional mixing process for laminar supersonic flows, the rate of diffusional mixing is related to the characteristic dimensions  $S_M$  of the jet nozzle, as well as the gas dynamic parameters  $p$  and  $T$  of the working medium. When the working medium conditions  $p$  and  $T$  are constant, it is most beneficial to accelerate the mixing process by reducing the lateral-direction mixing distance  $S_M$ .

Based on the above-mentioned analysis, the authors designed several jet nozzles with different  $S_M$ ; the detailed parameters are shown in Table 1. In the table,  $d_t$  is the diameter of the



Table 1 Elementary parameters of nozzles (calculated)

nozzle	$S_w$ (mm)	Primary nozzle				secondary nozzle			
		$d_i$ (mm)	$n$ (No)	$M$	$A_e/A_t$	$d_i$ (mm)	$M$	$A_e/A_t$	form of $H_2$ addition
CL-A	4.25	1.2	38	—	25	0.8	1	1	subsonic fine-hole
CL-11	3.40	1.0	115	5.3	20	0.5	4.7	20	supersonic fine-hole
CL-1	2.70	0.5	240	5.3	20	0.6	4.2	13	supersonic fine-hole
CL-9	1.75	0.3	450	5.3	20	0.3	3.9	11	supersonic fine-hole

jet nozzle throttle,  $n$  is the number of nozzles,  $M$  is the Mach number, and  $A_e/A_t$  is the nozzle exit area to the nozzle throttle area ratio. To find the lateral-direction velocity component of the gas flow and to increase the turbulence downstream of the nozzle exit, two different nozzle diffusion half-angles ( $11^\circ$  and  $15^\circ$ ) are considered. Different modes of hydrogen addition will have apparent different gas dynamic phenomena of the mixing layer. The authors designed two modes of hydrogen addition: one is hydrogen addition at supersonic speed in two-dimensional

Table 2 Parameters of supersonic two-dimensional split nozzle  $H_2$  addition

nozzle	$S_w$ (mm)	primary nozzle				secondary nozzle	
		$d_i$ (mm)	$n$ (No)	$M$	$A_e/A_t$	$h_i$ (mm)	$A_e/A_t$
CL-6	1.75	0.52	190	5.7	27	0.2	3.5
CL-7	1.75	0.52	232	5.3	20	0.2	4.5
CL-5	1.75	0.30	374	5.3	20	0.2	8

$$\delta^* = 0.0087x$$

slits, and another mode of hydrogen addition at supersonic speed in three-dimensional small holes. Table 2 shows the detailed

parameters. In the table,  $h_t$  is the height of the jet nozzle when hydrogen was added to two-dimensional slits.

For convenience in machining, type H62 brass was used as the nozzle material. To prevent reattachment of the F atoms onto the brass surface, nickel was deposited on the nozzle inner surface.

Relatively speaking, the boundary layer of the small-Reynolds'-number nozzle is relatively thicker; this is a problem that we cannot neglect. However, there is still a lack of a complete effective revision method on the additional surface layer for nozzles with three-dimensional holes. Therefore, the conventional empirical formula of the adherent layer of laminar flow [3] was used to revise the computed displacement thickens  $\delta^*$  at the nozzle exit. The revised formula is

$$\delta^*=0.0087x .$$

The flow calculation in the jet nozzle applies to the assumption of one-dimensional isentropic flow, regarding  $r$  in the flow process in the nozzle as constant. When calculating the mixing parameters and the exits of the primary and secondary nozzles, it is assumed that the mixing and reaction processes are independent. In other words, what first occurs is the mixing of flows from the primary and secondary nozzles, and then the reaction of the mixed gas flows. The reaction process is adiabatic, frictionless, and shock wave-free [4]. (This simplification may differ somewhat from the actual flow, but it can serve as a reference.) Tables 3 and 4 show the calculation results for type CL-9 nozzles.

Table 3 Operating condition and dimensions for CL-9 nozzle

parameter	symbol	units	primary nozzle	secondary nozzle
Mach number	$M$		5.2	3.9
pressure	$P_c$	torr	5	5
velocity	$u_c$	cm/s	$2176 \times 10^2$	$2554 \times 10^2$
temperature	$T$	K	169	74
density	$\rho$	g/cm <sup>3</sup>	$5.51 \times 10^{-6}$	$2.10 \times 10^{-6}$
mole fraction	$Y_F$		0.15	
	$Y_{DF}$		0.34	
	$Y_{He}$		0.51	
	$Y_{H_2}$			1
displacement thickness	$\delta^*$	cm	0.0023	0.0017
throat diameter	$d_t$	cm	0.030	0.030
exit diameter	$d_e$	cm	0.1340	0.1000
expansion half-angle	$\alpha$	degree	15	15.3
number of nozzle	$n$	No	450	450

The fundamental nozzle structure is of the integral type, without water cooling. This is feasible for experiments with short-term operation. Fig. 3 shows the schematic structure.

### III. Experimental Results and Discussion

All thermal experiments with the nozzles were conducted on a continuous-wave chemical laser device driven with a kilowatt-level combustion. In the experimental process, flows of the

Table 4 Operating condition (calculated) before and after mixing and reaction for CL-9

parameter	before mixing		after mixing	after reaction
	primary nozzle	secondary nozzle		
$M$	5.2	3.9	3.87	1.71
$T$ (K)	169	74	1.86	643
$T_0$ (K)	1600	298	811	1124

349

working media,  $F_2$ ,  $D_2$ , He, and  $H_2$  were measured; also measured were the combustion chamber pressure  $p_c$ , laser cavity pressure

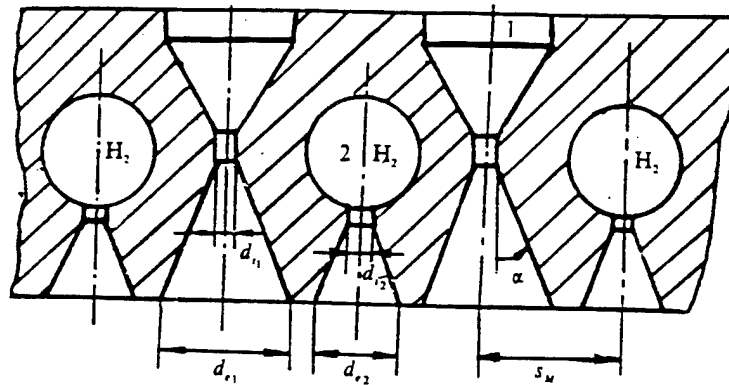


Fig. 3 Schematic of nozzle structure  
1. primary nozzle 2. secondary nozzle

$p_i$ , distance  $x_c$  between the optical axis and the nozzle exit, and the distributions along the gas flow direction of small-signal gain coefficient of  $p_i=1, 2$ , and 3 spectral lines in the laser cavity. The experimental conditions and results for several jet nozzles are shown in Tables 5 to 7 and also in Fig. 4. In the tables,  $F_2/D_2$  is the molar flow of  $F_2$  and  $D_2$  for  $F_2/D_2$  entering the combustion chamber;  $w_x$  is the total working medium flow; and the specific power is the ratio between the output power and the

total flow quantity  $W_{\Sigma}$ .

Table 5 Experimental condition and results for CL-A, CL-11, CL-1 and CL-9 nozzle

No	$S_M$ (mm) nozzle	experimental condition				condition of optical cavity			experimental results	
		$F_2/D_2$	$W_2$ (g/s)	$p_c$ (kg/cm <sup>2</sup> )	$p_L$ (torr)	reflection mirror	output mirror	$x_c$ (mm)	power (W)	specific power (J/g)
79-204	4.25 (CL-A)	1.68	8.09	2.37	3.5	R6 <sup>m</sup> spherecal	R6 <sup>m</sup> spherecal	20	567	70
80-318	3.40 (CL-11)	1.63	12.60	1.88	2.2	R6 <sup>m</sup> column	R6 <sup>m</sup> spherecal	20	1035	82
79-222	2.70 (CL-1)	1.48	7.81	2.30	3.0	R6 <sup>m</sup> column	R6 <sup>m</sup> spherecal	17	829	106
80-359	1.75 (CL-9)	1.44	7.84	3.65	3.0	R6 <sup>m</sup> column	R6 <sup>m</sup> spherecal	10	1025	130

From Fig. 5, we can see the following: (1) when the lateral-direction mixing distance  $S_N$  of the primary and secondary nozzles was reduced (4.55mm to 1.75mm), the specific power of the laser device increased from 70J/g to 130J/g. The reason is due to the reduction of the mixing distance  $S_M$  with accelerated mixing so that there is an increase in HF generated per unit time. This is consistent with the foregoing analysis. (2) When the lateral-direction mixing distance  $S_M$  was reduced and the mixing was accelerated, the characteristic mixing length becomes shorter, so that the position of the optical axis had to move forward from 20mm to 10mm from the nozzle exit so that the equivalent light release zone became shorter. In Fig. 4, as indicated with the gain distribution of the p branch, there was a positive gain

Table 6 Experimental results for CL-9 nozzle

No	experimental condition				condition of optical cavity			experimental results	
	$F_1/D_1$	$W_1$ (g/s)	$p_1$ (kg/cm <sup>2</sup> )	$p_L$ (torr)	reflection mirror	output mirror	$x_c$ (mm)	power (W)	specific power (J/g)
80-354	1.41	7.96	3.55	3.0	R6 <sup>m</sup> column	R6 <sup>m</sup> spherical	10	959	120
80-355	1.42	7.84	3.60	3.0	R6 <sup>m</sup> column	R6 <sup>m</sup> spherical	10	917	117
80-356	1.41	7.98	3.65	3.0	R6 <sup>m</sup> column	R6 <sup>m</sup> spherical	10	934	117
80-357	1.43	7.84	3.65	3.0	R6 <sup>m</sup> column	R6 <sup>m</sup> spherical	10	933	119
80-358	1.44	7.83	3.65	3.0	R6 <sup>m</sup> column	R6 <sup>m</sup> spherical	10	955	122
80-359	1.44	7.84	3.65	3.0	R6 <sup>m</sup> column	R6 <sup>m</sup> spherical	10	1025	131
80-360	1.44	7.84	3.65	3.0	R6 <sup>m</sup> column	R6 <sup>m</sup> spherical	10	933	119

coefficient in the type CL-9 nozzle only in the range of approximately 2cm. At further distances, it became an absorption region.

From Table 7 we can see that, with respect to the same nozzle throttle dimensions, although the distance  $S_M$  was reduced for mixing in the lateral-direction, yet since the two-dimensional hydrogen addition was applied, the specific power was reduced by nearly 20%. However, for type CL-05 and type CL-9 nozzles with  $d_t=0.3\text{mm}$ , the lateral-direction mixing distance was 1.75mm, but the specific power was 38% less. This occurred mainly when there was hydrogen addition at the two-dimensional

Table 7 Comparison between two-dimensional split nozzle and three dimensional fine-hole  $H_2$  addition

No	nozzle	$d_i$ (mm)	experimental condition				condition of optical cavity			experimental results	
			$F_2/D_2$	$W_2$ (g/s)	$P_e$ (kg/cm <sup>2</sup> )	$P_i$ (torr)	reflection mirror	output mirror	$x_i$ (mm)	power (W)	specific power (J/g)
80-008	CL-1 <sup>a</sup>	0.5	1.44	8.71	3.20	2.5	R6 <sup>m</sup> spherical	R10 <sup>m</sup> spherical	13	881	101
80-119	CL-6	0.5	1.42	9.05	3.20	/	R6 <sup>m</sup> spherical	R10 <sup>m</sup> spherical	10	721	80
80-097	CL-7	0.5	1.47	9.26	2.65	2.0	R6 <sup>m</sup> spherical	R10 <sup>m</sup> spherical	13	730	79
80-156	CL-5	0.3	1.31	7.85	4.60	2.0	R6 <sup>m</sup> spherical	R10 <sup>m</sup> spherical	10	638	81
80-359	CL-9 <sup>a</sup>	0.3	1.44	7.84	3.65	3.0	R6 <sup>m</sup> spherical	R6 <sup>m</sup> spherical	10	1025	130

<sup>a</sup> Supersonic three-dimensional fine hole  $H_2$  addition.

slits, the length of the mixing surface of the gas flow from the primary and secondary nozzles was smaller than in the three-dimensional case. Moreover, the nozzle expansion ratio was smaller for hydrogen addition at the two-dimensional slits. During the experiment, the pressures at the exits of the primary and secondary nozzles were seriously mismatched so that the gas dynamic conditions of the flow field deteriorated.

#### IV. Conclusions

When using a three-dimensional, small-hole nozzle array for a combustion-driven HF chemical laser device, it was beneficial to upgrade the specific power of the HF laser device to reduce the lateral-direction mixing distance between the primary and the secondary nozzles and to adopt hydrogen addition with three-

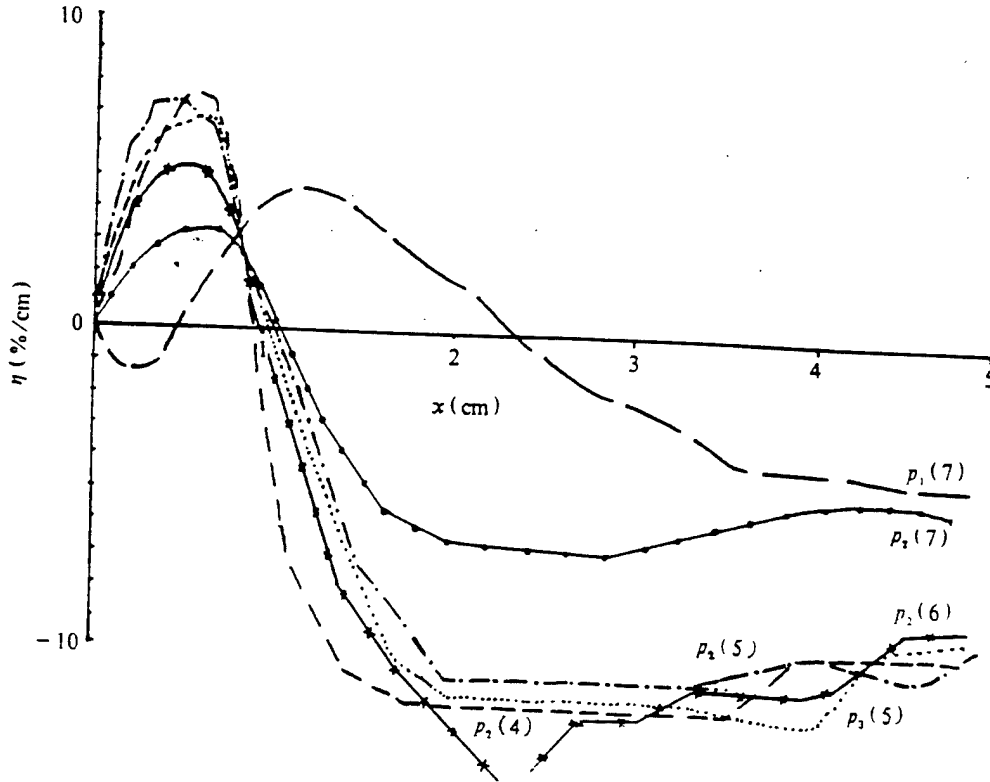


Fig. 4 Distribution of small signal gain coefficient along the direction of gas flow for CL-9 nozzle

dimensional supersonic speed. As indicated in the experiments, when the array  $S_M$  was reduced from 4.25mm to 1.75mm, the corresponding throttle diameter of the primary and secondary nozzles was reduced from 1.2mm to 0.3mm, and the specific power of the HF laser device was upgraded from 70J/g to 130J/g.

The authors are grateful to Fang Jingke, Li Mingsheng, Min Xiangde, Wang Kaili, Sun Mingzhu, Heng Changqing, and Xu Qingzhou et al., for participating in the research.

The first draft of the article was received on July 17, 1990; the final revised draft was received for publication on September 26, 1990.



DISTRIBUTION LIST

DISTRIBUTION DIRECT TO RECIPIENT

ORGANIZATION

MICROFICHE

BO85 DIA/RTS-2FI	1
C509 BALL0C509 BALLISTIC RES LAB	1
C510 R&T LABS/AVEADCOM	1
C513 ARRADCOM	1
C535 AVRADCOM/TSARCOM	1
C539 TRASANA	1
Q592 FSTC	4
Q619 MSIC REDSTONE	1
Q008 NTIC	1
Q043 AFMIC-IS	1
E404 AEDC/DOF	1
E410 AFDTC/IN	1
E429 SD/IND	1
P005 DOE/ISA/DDI	1
1051 AFIT/LDE	1
PO90 NSA/CDB	1

Microfiche Nbr: FTD96C000363  
NAIC-ID(RS)T-0136-96